

Journal of Materials Chemistry A

Materials for energy and sustainability

Accepted Manuscript

This article can be cited before page numbers have been issued, to do this please use: F. Li, Z. Liu, J. Shen, X. Xu, L. Zeng, B. Zhang, H. Zhu, Q. Liu, J. Liu and M. Zhu, *J. Mater. Chem. A*, 2021, DOI: 10.1039/D0TA10608A.



This is an Accepted Manuscript, which has been through the Royal Society of Chemistry peer review process and has been accepted for publication.

Accepted Manuscripts are published online shortly after acceptance, before technical editing, formatting and proof reading. Using this free service, authors can make their results available to the community, in citable form, before we publish the edited article. We will replace this Accepted Manuscript with the edited and formatted Advance Article as soon as it is available.

You can find more information about Accepted Manuscripts in the [Information for Authors](#).

Please note that technical editing may introduce minor changes to the text and/or graphics, which may alter content. The journal's standard [Terms & Conditions](#) and the [Ethical guidelines](#) still apply. In no event shall the Royal Society of Chemistry be held responsible for any errors or omissions in this Accepted Manuscript or any consequences arising from the use of any information it contains.

Nanorod-like Ni-rich layered cathode with enhanced Li⁺ diffusion pathway for high-performance lithium-ion batteries

Fangkun Li^a, Zhengbo Liu^a, Jiadong Shen^a, Xijun Xu^a, Liyan Zeng^a, Binghao Zhang^b, He Zhu^b, Qi Liu^{b,*}, Jun Liu^{a,*}, Min Zhu^a

^aGuangdong Provincial Key Laboratory of Advanced Energy Storage Materials, School of Materials Science and Engineering, South China University of Technology, Guangzhou 510641, P. R. China, E-mail: msjliu@scut.edu.cn

^bDepartment of Physics, City University of Hong Kong, Hong Kong 999077, P. R. China, E-mail: qiliu63@cityu.edu.hk

Abstract

Ni-rich LiNi_xCo_yMn_{1-x-y}O₂ (x ≥ 0.6) layered oxide cathodes are one of the most promising cathode materials for lithium-ion batteries (LIBs) owing to their superior capacity, prominent energy density and low cost. However, the large volume change caused by phase transition and poor diffusion kinetics limits its application. Herein, a nanorod-like Ni-rich layered LiNi_{0.6}Co_{0.2}Mn_{0.2}O₂ cathode is synthesized via a facial surfactant-free co-precipitation route. Due to the unique nanorod morphology, more {010} electrochemical active planes are exposed. As a result, structural stability and diffusion kinetics are improved a lot. In terms of performance, it exhibits outstanding structural stability (the volume change is as small as 2.12% in the processes of charging and discharging) and rate performance (achieve a high discharge capacity of 152.2 mAh g⁻¹ at 5 C). Such rational designed cathode could meet the high high-energy

requirements of the next generation LIBs.

View Article Online
DOI: 10.1039/D0TA10608A

Keywords: Li-ion batteries, Ni-rich layered cathode, diffusion kinetics, volume change

1 Introduction

Pursuing the efficient use of environmentally friendly and low carbon emission clean energy has been stimulating a wide range of research interests on lithium-ion batteries (LIBs).¹⁻⁵ At present, electric vehicles (EVs) are widely used in our life causing a daily-increasing demand for high energy density LIBs.⁶⁻⁸ It is well known that the cathode is an indispensable component, which considerably determines the whole energy density of batteries. To meet market demands, the development of high-capacity cathode materials is an irresistible trend. In this regard, Ni-rich $\text{LiNi}_x\text{Co}_y\text{Mn}_{1-x-y}\text{O}_2$ ($x \geq 0.6$) layered cathodes have been attracting significant attention because of their superior capacity, environment temperately and low cost.⁹⁻¹¹ Unfortunately, these layered oxides suffer from intrinsic low rate capability, severe capacity fade, and rapid voltage decay leading to sluggish Li^+ ion transport dynamics.¹² To overcome these issues, a wide range of strategies have been proposed and investigated to enhance the chemical and structural stabilities by surface engineering,^{13, 14} element doping,¹⁵⁻¹⁸ and morphology control.¹⁹⁻²⁵

To date, one-dimensional (1D) nanostructures, including nanorods,²⁶ nanowires,²⁷⁻²⁹ nanotube arrays^{30, 31} and nanobelts,³² etc., have been widely investigated to improve the electrochemical performances of electrode materials. Particularly, the unique morphology of 1D electrode can offer short electron/ion transport distance and strong

tolerance to stress change, thus deliver high capacity, superior rate performance and long-term cycling. Generally, the relationship between the Li^+ diffusion coefficient (D_{Li^+}) and the transportation length (L) abides the Eq. (1):³³

$$\tau = \frac{L^2}{D_{\text{Li}^+}} \quad (1)$$

Where τ is diffusion time in electrode materials. The nanosized primary particles in 1D nanomaterials can shorten the transmission length (L) of Li^+ , thus decrease the diffusion time (τ), resulting in enhanced Li^+ diffusion kinetics of LIBs, remarkably improving the rate performance. Certainly, many previous research results revealed that the nanosized materials with enhanced electrochemical dynamics could efficiently improve the rate performance. For example, Winter et al. proved that a major part of the overall specific capacity loss was induced by kinetic limitations,³⁴ and Passerini et al. verified that it was beneficial to enhance the rate performance by synthesis 1D nanomaterials. Its unique structure could offer fast Li^+ ion transport pathways, thus significantly enhancing the lithium-ions diffusion kinetics.³⁵

Over and above that special structure design, another clever strategy to resolve the sluggish Li^+ transportation is that expose more electrochemical active planes (*i. e.*, $\{010\}$ planes).^{36–38} In principle, Ni-rich NCM cathode possesses a typical hexagonal α - NaFeO_2 type structure with $R\bar{3}m$ space group providing 2D channels for Li^+ diffusion along either a - or b -axis. The densely packed MO_6 ($M=\text{Ni, Co, Mn}$) octahedral perpendicular to the c -axis form the MO_2 layers (*i. e.*, $\{001\}$ facets) that are inactive electrochemical facets impeding the Li^+ transporting.³⁹ By contrast, the six equivalent side planes of (100) , $(\bar{1}00)$, $(0\bar{1}0)$, (010) , $(1\bar{1}0)$ and (110) denoted by $\{010\}$ planes,

which are considered as the favorable electrochemical active planes offering an open structure for Li^+ diffusion.²³ Nevertheless, it is still a huge challenge that fabricates layered structure cathode with more exposed $\{010\}$ active planes, because the surface free energy of $\{010\}$ planes is higher than that of the $\{001\}$ ones.⁴⁰ An effective strategy was that adding a surfactant to slowing down the crystal growth rate of $\{001\}$ facets and thus achieving the Ni-rich cathode with more exposed $\{010\}$ active planes. Recently, many surfactants have been adopted to control the morphology of Ni-rich cathode with more exposed electrochemical active planes, such as polyethylene glycol (PEG),^{26, 32} polyvinylpyrrolidone (PVP),⁴¹ and sodium dodecyl sulfate (SDS),^{36, 42} and so on. However, the addition of organic surfactants (PEG, PVP, and SDS, etc.) undoubtedly increases the synthetic cost and thus hampering its practical applications. Although, $\text{LiNi}_{0.8}\text{Co}_{0.1}\text{Mn}_{0.1}\text{O}_2$, $\text{LiNi}_{1/3}\text{Co}_{1/3}\text{Mn}_{1/3}\text{O}_2$, $\text{Li}_{1.2}\text{Ni}_{0.2}\text{Mn}_{0.6}\text{O}_2$ and $\text{NaLi}_{0.05}\text{Ni}_{0.3}\text{Mn}_{0.5}\text{Cu}_{0.1}\text{Mg}_{0.05}\text{O}_2$ with exposed $\{010\}$ active planes have been successfully synthesized and greatly studied. To the best of our knowledge, synthesis of nano-like $\text{LiNi}_{0.6}\text{Co}_{0.2}\text{Mn}_{0.2}\text{O}_2$ with exposed $\{010\}$ active facets via a surfactant-free route has never been published.

Herein, a nanorod-like Ni-rich layered cathode of $\text{LiNi}_{0.6}\text{Co}_{0.2}\text{Mn}_{0.2}\text{O}_2$ with prominent exposed $\{010\}$ electrochemical active facets has been synthesized via a facial surfactant-free oxalate precursor crystallization route combined with a solid lithiation treatment. The *in-situ* synchrotron high-energy X-ray diffraction (HEXRD) technique exhibits that the Ni-rich $\text{LiNi}_{0.6}\text{Co}_{0.2}\text{Mn}_{0.2}\text{O}_2$ has a stable lattice structure and strong tolerance to stress changes during the charge/discharge process (the unit cell

volume change is as small as 2.12%). Moreover, the synergistic effect between exposure {010} electrochemical active surface and nanometer size dramatically shorten the Li⁺ diffusion pathways and thus enhance diffusion kinetics improving the rate performance.

2 Experimental section

Material Synthesis

Preparation of the MC₂O₄ · xH₂O precursor

In a typical process, 12 mmol of Ni(CH₃COO)₂·4H₂O, 4 mmol Co(CH₃COO)₂·4H₂O 4 mmol Mn(CH₃COO)₂·4H₂O and 23 mmol of LiCH₃COO·2H₂O were dissolved in 200 ml binary solvent system with ethanol-water (ethanol: water= 4:1 v/v) under continuous stirring to form transparent solution A. On the other hand, 40 mmol H₂C₂O₄·2H₂O) was poured into another 200 ml mixture solution (the same as the above solution) under vigorous stirring to obtain colorless clear solution B. Then, the solution B was injected into A with stirring for another 6 h. After that, the MC₂O₄ · xH₂O (M= Li, Ni, Co, Mn) nanorods were collected by evaporating the solvents and drying the as-prepared pink precipitate in an air-dry oven at 80 °C for 18 h.

Preparation of the nanorod-like LiNi_{0.6}Co_{0.2}Mn_{0.2}O₂ cathode

The as-obtained MC₂O₄ · xH₂O nanorods precursor was pre-treated in a muffle furnace at 450 °C for 8 h and then temperature raised to 800 °C for 15 h to obtain the layered nanorod-like LiNi_{0.6}Co_{0.2}Mn_{0.2}O₂ cathode (marked as N-NCM).

Materials Characterization

The crystal information of as-prepared powder was performed on a PANalytical Empyrean X-ray diffraction (XRD) at 40 kV with a measurement current of 45 mA and equipped with a Cu-K radiation source. The measured data of XRD were in-depth analyzed by the Rietveld refinement program-General Structure Analysis System (GSAS) software. Fourier Transform Infrared Spectroscopy (FT-IR) spectra were collected using an FT-IR Nicolet IS50 instrument for 4000 to 400 cm^{-1} . The as-prepared products were mixed with KBr powder for FT-IR measurements. Background correction was made using a blank KBr pellet as the reference. TG was characterized by Q50 thermogravimetric analyzer from 40 to 800 $^{\circ}\text{C}$ at 10 $^{\circ}\text{C min}^{-1}$ in O_2 atmosphere. Morphology of as-prepared N-NCM was revealed by a Scanning Electron Microscope (SEM, Zeiss Gemini DSM 982). The microstructures and elemental distribution of as-prepared products were observed by a JEOL 2100F Transmission Electron Microscope (TEM) at 200 kV. The valence states of Ni, Co and Mn in N-NCM cathode were performed by X-ray photoelectron spectroscopy (XPS) with ThermoFisher ESCALAB XI+ system (Al $\text{K}\alpha$ radiation, 1486.6 eV). To compare the thermal stability of N-NCM and commercial $\text{LiNi}_{0.6}\text{Co}_{0.2}\text{Mn}_{0.2}\text{O}_2$ (C-NCM) cathodes, DSC was recorded from 40 to 350 $^{\circ}\text{C}$ using a TA-Q20 Differential Scanning Calorimetry with a heating rate of 5 $^{\circ}\text{C min}^{-1}$. For the DSC tests, the cathode materials were charged to 4.4 V vs Li/Li⁺ at C/10 rate and then disassembled and washed with diethyl carbonate (DEC) solvent three times in an Ar-filled glove box. After that, scratching the powders from the dried electrodes package into high-pressure crucibles with electrolyte. *In-situ* synchrotron

XRD measurements were carried out at 11-ID-C beamline with the X-ray wavelength of 0.1173 Å at Advanced Photon Source (APS), Argonne National Laboratory (ANL), and Si (113) single crystal was employed as the monochromator of an X-ray beam at 105.7 keV. The coin cells have a hole in the middle, which is convenient for the X-ray directly irradiating the N-NCM electrode. During the test process, the charge-discharge current density of the cell was C/10 rate, and the data collection time for a single XRD pattern was within 8 s. The original two-dimensional diffraction data was collected by a Perkin-Elmer detector, and they were integrated and calibrated via Fit2D software. All the XRD patterns were refined and corresponding lattice parameters were extracted using Fullprof software.⁴³ In detail, the backgrounds were removed by linear interpolation and the peak shapes were demonstrated through the Thompson-Cox-Hastings profile function when using the Le Bail method.

Electrochemical Measurements

For working electrodes, N-NCM (or C-NCM), polyvinylidene fluoride (PVDF) and Super P with a weight ratio of 8: 1: 1 were mixed in a mortar with N-methyl-2-pyrrolidinone (NMP) to get a homogeneous slurry and then spread on a clean Al foil and dried in a vacuum oven at 100 °C for overnight. Then, the electrode was cut into 12-mm disks with the active mass loading around $2.3 \pm 0.2 \text{ mg cm}^{-2}$. The test CR2025 coin-type cells were assembled in an Ar-filled glove box with both H₂O and O₂ < 0.01 ppm. 1M LiPF₆ dissolved in EC: DMC: EMC (1: 1: 1 in volume) used as the electrolyte, Li foil as counter-electrode and polypropylene as separators. Galvanostatic testing of

the cells was charged/discharged between 2.8 and 4.4 ~ 4.6 V (vs Li/ Li⁺) at 30 and 60 °C using a Land 2001A testing system. CV and EIS curves were collected on an electrochemical workstation (Gamry Interface 1000). CV curves were tests at 0.1 mV s⁻¹ in a voltage range of 2.8–4.4 V. EIS profiles were recorded with an amplitude of 5 mV from 10⁵ Hz to 10⁻². The GITT was performed with a constant current pulse for 10 min at C/10 rate and then rest for 1 h.

3 Results and Discussion

Fig. 1a demonstrates the preparation steps of nanorod-like LiNi_{0.6}Co_{0.2}Mn_{0.2}O₂ (N-NCM), including a co-precipitation step in the ethanol-water system and followed by a solid lithiation treatment. Firstly, the uniform hydrated metal oxalates MC₂O₄·xH₂O (M= Li, Ni, Co, Mn) precursor was acquired via a simple surfactant-free co-precipitation method. Subsequently, the as-synthesized MC₂O₄·xH₂O precursor directly annealing in a furnace under air condition to obtain the N-NCM nanorod. The SEM signal of the precursor (Fig. 1b) reveals that the MC₂O₄·xH₂O possesses a nanorod-like morphology with a width of ~400 nm and a length of ~3 μm. The XRD pattern (Fig. S1) and FT-IR spectrum (Fig. S2) prove that the as-obtained precursor is composed of Li₂C₂O₄ and (Ni, Co, Mn)C₂O₄·2H₂O⁴⁴ To well-inherit the morphology of precursor and rational design the lithiation procedure, the TG/DTG result of MC₂O₄·xH₂O was also measured (Fig. S3). The SEM results of the final product (Fig. 1c) suggest that the N-NCM final product well-preserved the shape of MC₂O₄·xH₂O nanorods. Also, the morphology characterization of commercial LiNi_{0.6}Co_{0.2}Mn_{0.2}O₂

(marked as C-NCM) cathode was performed and compared with the designed N-NCM.

The SEM image (Fig. S4) shows the C-NCM particles with an average size of $\sim 2 \mu\text{m}$ and corresponding SEM-EDS mapping signals (Fig. S5) reveal that all the elements are uniformly distributed. Fig. S6 displays the N_2 adsorption/desorption isotherms of N-NCM and C-NCM cathode and the surface area of N-NCM can be calculated as $3.315 \text{ m}^2 \text{ g}^{-1}$ which is higher than that of C-NCM ($1.014 \text{ m}^2 \text{ g}^{-1}$).

The structural characterization of N-NCM and C-NCM were collected by the powder X-ray diffraction (XRD) pattern and depicted in Fig. 1d and Fig. S6b, which are well matched with hexagonal $\alpha\text{-NaFeO}_2$ structure (space group, $R\bar{3}m$) without impurity phase. The crystallographic and atomic site information of N-NCM and C-NCM received from the Rietveld refinements are listed in Table S1-4. Compared to C-NCM, the N-NCM exhibits smaller lattice parameters a and c indicating that the N-NCM cathode has a better crystallinity.¹⁸ The intensity ratios ($I_{(003)}/I_{(104)}$) of N-NCM and C-NCM are both larger than 1.2, which demonstrates the slight degree of $\text{Li}^+/\text{Ni}^{2+}$ mixed cationic.^{45, 46} Furthermore, the splits of (006)/(102) and (018)/(110) reveal that the Ni-rich layered oxides possess a highly ordered structure. The intensity ratio value of $I_{(110)}/I_{(018)}$ of the N-NCM is 1.07 from the XRD patterns (Fig. 1d) which are higher than that of C-NCM (0.96, Fig. S7c). A bigger value of $I_{(110)}/I_{(018)}$ indicates that N-NCM has $\{010\}$ oriented active facets caused by the faster growth of these high-energy facets.^{36, 47-50} As shown in Fig. S8, the (110) planes have an open layered interspace for the Li^+ transporting. But for (108) planes, there are no straight tunnels for Li^+ diffusion owing to the dense stacking of atoms. To verify the morphology characteristics and the

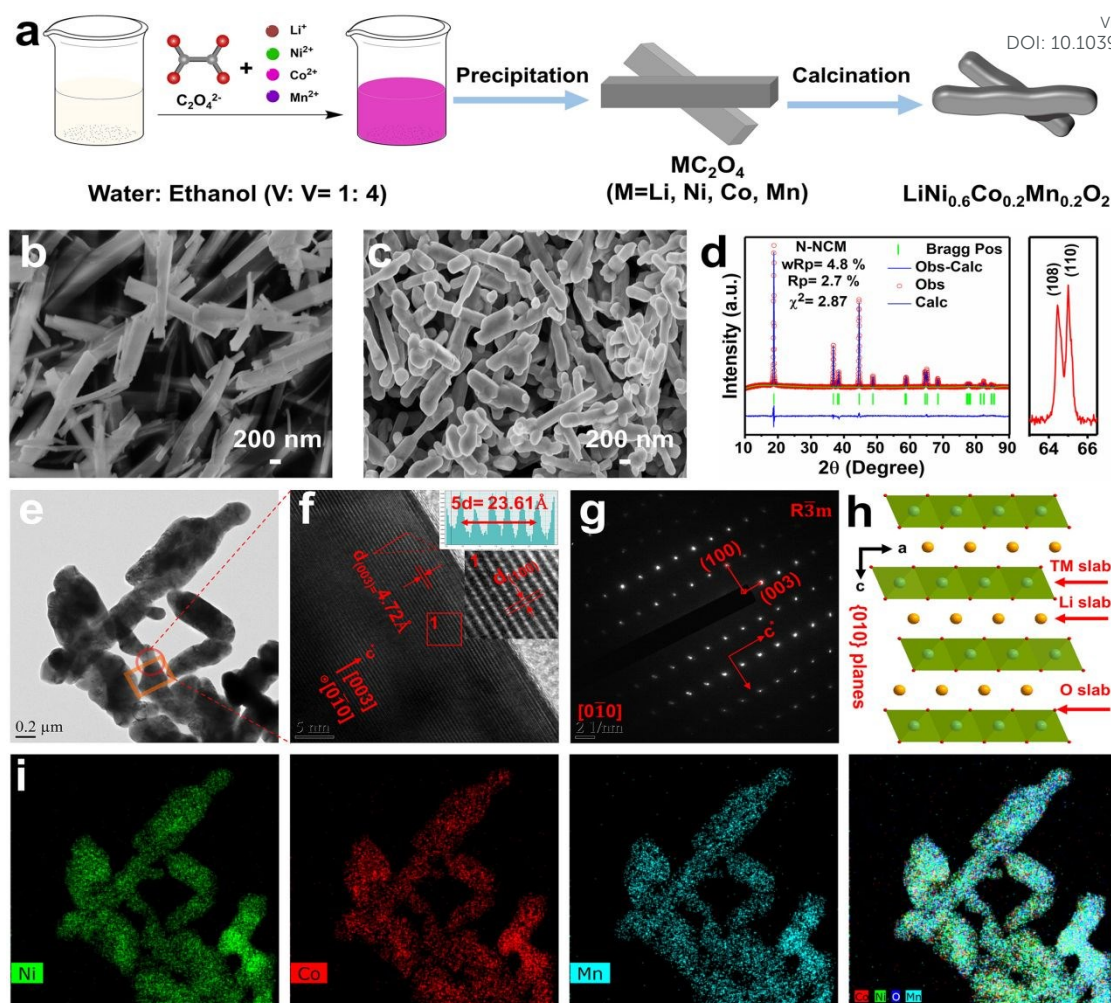


Fig. 1. (a) Schematic illustration for the preparation of nanorod-like $\text{LiNi}_{0.6}\text{Co}_{0.2}\text{Mn}_{0.2}\text{O}_2$ (N-NCM) cathode; (b, c) SEM images of the nanorod-like $\text{MC}_2\text{O}_4 \cdot x\text{H}_2\text{O}$ (M= Ni, Co, Mn, Li) precursor and N-NCM cathode; (d) refined XRD patterns of N-NCM cathode based on LiNiO_2 hexagonal ($R\bar{3}m$) phases and enlarged view of (108) and (110) peaks; (e-g) TEM, HRTEM images, and SAED pattern of the N-NCM cathode; (h) crystal structure of N-NCM cathode; (i) elemental EDS mapping of Ni, Co, Mn, and all elements.

lattice structure of N-NCM, the high-resolution transmission electron microscope (HRTEM) and selected area electron diffraction (SAED) measurements were

performed. The TEM image of N-NMC (Fig. 1e) displays a nanorod-like shape, which is consistent with the SEM results (Fig. 1d). The HRTEM image (Fig. 1f) exhibits clear lattice fringes with an interplanar spacing of 4.72 Å, which can be assigned to the (003) planes. Combined with the corresponding SAED patterns (Fig. 1g), it is confirmed that these N-NCM nanorods with a hexagonal layered structure. Furthermore, the lattice fringes of region 1 in Fig. 1f displays an interplanar distance of 2.80 Å, which can be indexed to the (100) planes. This demonstrates that the lateral plane was classified to the {010} electrochemical active facets (parallel to the c-axis direction), which can offer more unobstructed pathways for fast Li⁺ insertion and extraction. In addition, the easily recognizable crystalline structure schematic of N-NCM is illustrated in Fig. 1h. As displayed in Fig. S9, the nanorod-like N-NCM cathode with preferred orientation {010} facets is also verified by SAED patterns characterization. To check the elemental composition of N-NCM, TEM-EDS elemental mapping was also collected. Fig. 1i exhibits the EDS mappings signals of Ni, Co, Mn, and O elements reveal that all these elements are evenly distributed. In summary, the 1D N-NCM nanorods were successfully obtained by controlling the growth of {010} planes via a rational design of the synthesis procedure. The X-ray photoelectron spectroscopy (XPS) characterization was performed to investigate the valence state of Ni, Co, and Mn elements. Fig. S10 displays the wide scan spectrum of N-NCM confirming the co-existence of C, O, Mn, Co and Ni elements. As exhibited in Fig. S10b-d, the characteristic peaks centred at 853.5/854.7, 780.1 and 641.9 eV could be assigned to the Ni²⁺/Ni³⁺, Co³⁺ and Mn⁴⁺, respectively.^{25, 51, 52}

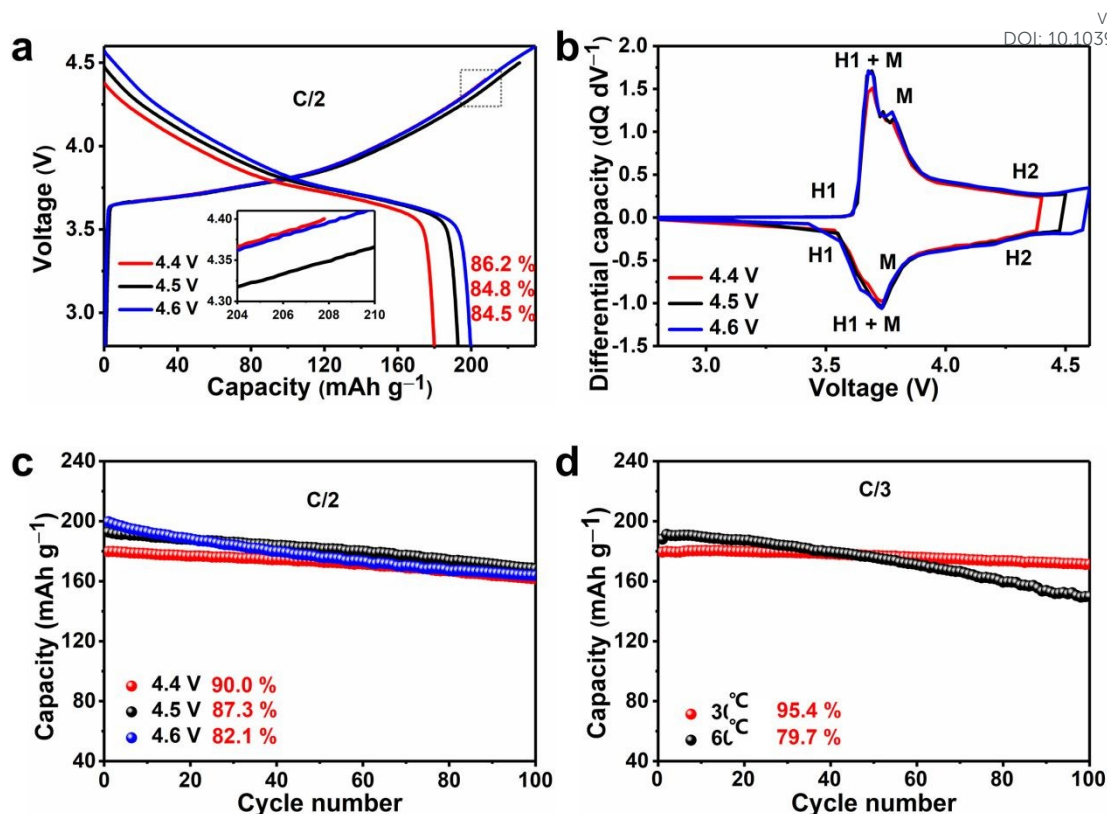


Fig. 2. Electrochemical performances of the N-NCM cathode: (a) the charge-discharge profiles of the first cycle at C/2 (1 C= 180 mAh g⁻¹) rate between 2.8 and 4.4–4.6 V at 30 °C; (b) differential capacity profiles of the first charge-discharge cycle; (c) long-term cycling performances at C/2 rate between 2.8 and 4.4–4.6 V; (d) cycling performances at C/3 rate in the voltage range of 2.8–4.4 V at 30 and 60 °C.

As displayed in Fig. 2 and Fig. S11., the cycling performances of N-NCM electrodes are measured under 2.8–4.4 V, 2.8–4.5 V and 2.8–4.6 V at a C/2 rate (1 C= 180 mA g⁻¹) in 30 °C conditions. The initial charge-discharge profiles of N-NCM (Fig. 2a) at different potential region indicates that with the cut-off voltage increases, the capacity increases. Furthermore, at a high cut-off voltage of 4.6 V, this N-NCM cathode possesses a high initial Coulombic efficiency of 84.5% and a high-capacity retention

rate of 82.1% after 100 cycles. To further unveil the charge/discharge mechanism, the relevant differential capacitance ($dQ \cdot dV^{-1}$) curves of N-NCM as a function of the cell voltage was provided in Fig. 2b. These profiles are typically characterized by two couples of redox peaks (even at 4.6 V cut-off voltage) and small redox reaction potential difference. This phenomenon is associated with the structural transition of N-NCM with a biphasic region from hexagonal to monoclinic (H1 to M) and a monoclinic to hexagonal (M to H2) during the Li^+ extraction/insertion.⁵³⁻⁵⁵ On account the working temperature plays a vital role in the battery health and life, the N-NCM electrode was also tested at both 30 and 60 °C (Fig. 2d and Fig. S12). Evidently, the N-NCM cathode possesses capacity retention of 95.4% and 79.7% after 100 cycles in the voltage region of 2.8–4.4 V at 30 °C and 60 °C, respectively.

To evaluate the advantages of this nanorod cathode, the electrochemical performance comparison of N-NCM and C-NCM was also performed. Fig. 3a,b show the results of cyclic voltammetry (CV) characterization, in which the initial oxidation/reduction peaks ($\text{Ni}^{2+}/\text{Ni}^{4+}$ redox processes) of N-NCM and C-NCM are situated at 3.898/3.653 V and 3.924/3.629 V, respectively. Moreover, it can be checked that the peak separation of the N-NCM cathode at a lower 0.245 V in the first cycle indicates a smaller polarization degree of the N-NCM cathode.⁴⁶ These results suggest that the Li^+ (de)intercalation in the N-NCM cathode is easier. The rate capabilities of these two samples were further studied at from C/10 to 5 C in a potential range of 2.8–4.4 V (Fig. 3c). It is evident that the N-NCM achieves a higher capacity and better rate capability than C-NCM in all the tests. Even at a 5 C rate, the N-NCM electrode still delivers a

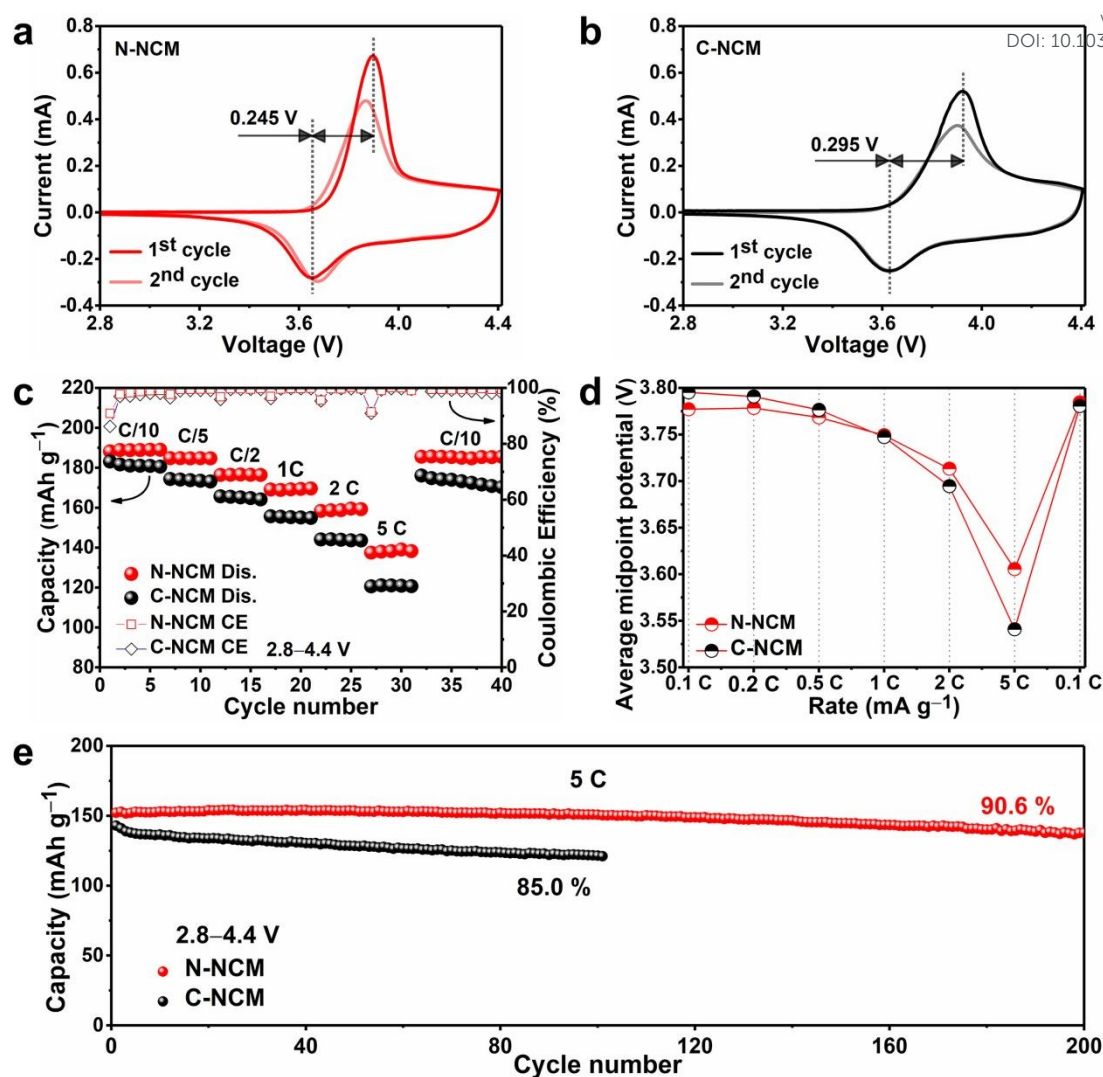


Fig. 3. The Li^+ storage properties of the N-NCM (red line) and C-NCM (black line) cathodes in the range of 2.8–4.4 V at 30 °C: (a,b) the CV profiles at 0.1 mV s^{-1} for initial two cycles; (c) rate capability at different charge-discharge rates (C/10, C/5, C/2, 1 C, 2 C, and 5 C) (Dis.: discharge, CE: Coulombic efficiency); (d) average midpoint potential at different charge-discharge rates; (e) cycling stability at 5 C.

discharge capacity of $\sim 138 \text{ mAh g}^{-1}$, which is much higher than that of C-NCM ($\sim 120 \text{ mAh g}^{-1}$). Besides, N-NCM displays better cycling stability and higher capacity than C-NCM when it returns to the C/10 rate. Fig. 3d shows the average midpoint potentials

at each C-rates of N-NCM and C-NCM. Obviously, when the current density increases to 5 C, the voltage drop of N-NCM (0.17 V) is much lower than that of C-NCM (0.26 V). Fig. S13 shows the corresponding charge-discharge curves and differential discharge capacity curves suggest that N-NCM better electrochemical performance and has smaller polarization.

Based on the above results, the cycling stability is also tested at 5 C in the voltage range of 2.8–4.4 V and offered in Fig. 3e and Fig. S14a–c. Obviously, N-NCM has a discharge capacity of 152.2 mAh g⁻¹, which is higher than that of C-NCM (143.0 mAh g⁻¹). It's noted that the N-NCM still has a high reversible capacity of 90.6% after 200 cycles but for C-NCM only 85.0% after 100 cycles. To investigate the intrinsic characteristics of N-NCM undergoes during the cycling process, the corresponding differential capacity versus voltage (dQ/dV) curves of the 1st, 50th, 100th, 150th, and 200th cycles at 5 C was conducted. As shown in Fig. S14d, it is evident verified that no new phase transition appears in the long-term cycles even at high current rates of 5 C. Simultaneously, the XRD pattern validates that the N-NCM cathode still possesses a complete hexagonal layered structure ($R\bar{3}m$, space group) (Fig. S15a). The EIS results after 200th cycles (Fig. S15b) with a larger value than the initial one indicates the deteriorating of Li⁺ diffusion kinetics and also explains the small capacity decay during the cycling process.^{34, 56, 57}. Notably, the N-NCM cathode also achieved excellent cycle stability at 2 C for 100 cycles (Fig. S16). Compared to the electrochemical performance with other reported LiNi_{0.6}Co_{0.2}Mn_{0.2}O₂-based materials (Table S5), the N-NCM nanorods cathode exhibit a better high-rate capability and more stable long cycle life.

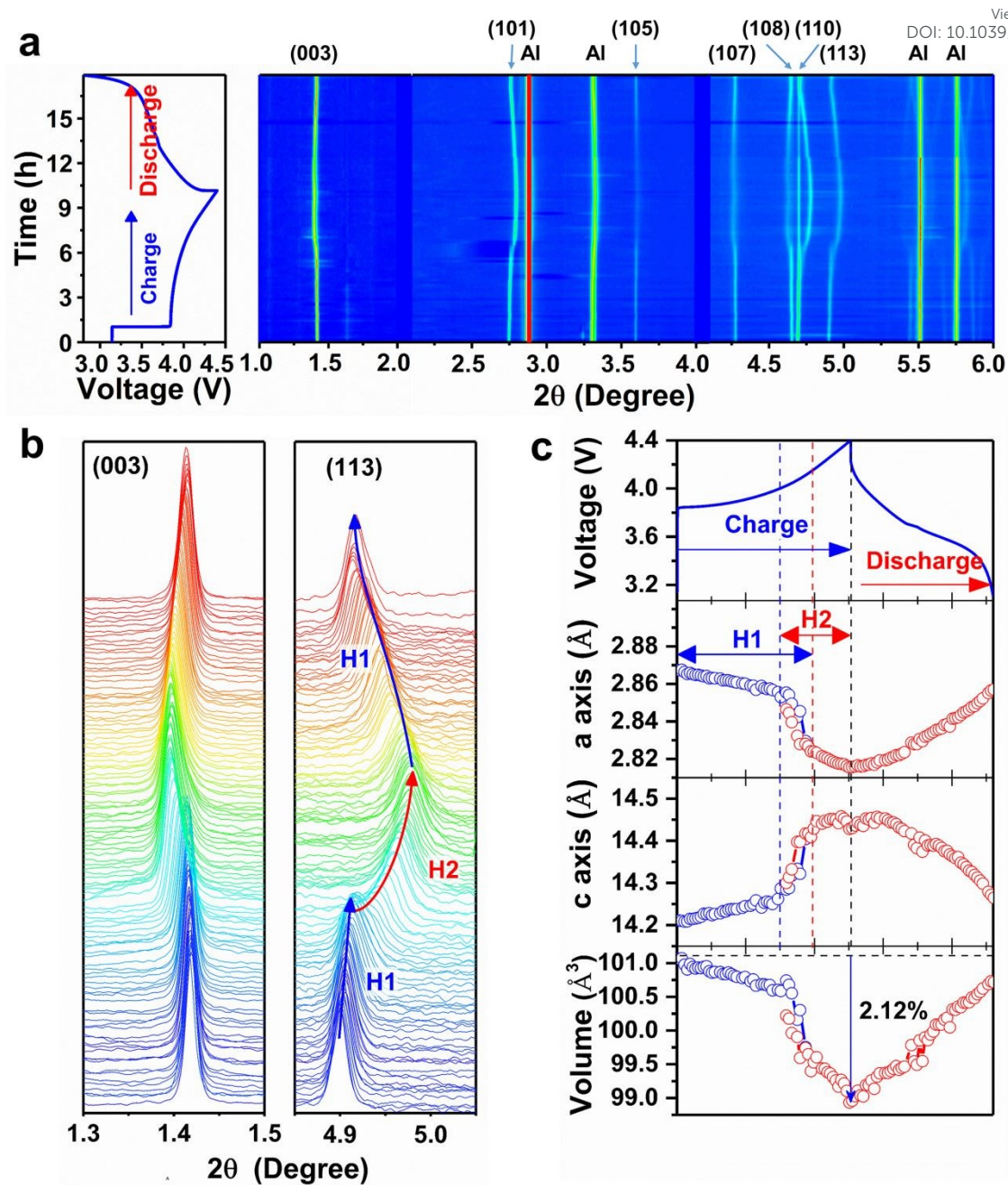


Fig. 4. (a) *In-situ* synchrotron XRD patterns of the first charge and discharge of N-NCM cathode between 2.8 and 4.4 V at a C/10 rate. Cell potentials are given at the left of the figure; (b) enlarged view of (003) and (113) peaks; (c) lattice constants evolution and unit cell volume change of N-NCM cathode as a function of time during the first cycle.

These test results indicate that the more exposed {010} active planes enhanced the diffusion kinetic by reducing the transport distance, thus improving the rate performance and cycling stability.

In-situ synchrotron XRD was further performed to understand the superior high-rate capability and long-term cycling performance of the N-NCM cathode. The obtained XRD patterns of N-NCM were fitted to reveal the evolution of phases and change of lattice parameters. The refined initial *in-situ* XRD result was provided in Fig. S17 and the corresponding lattice parameters extracted from each XRD pattern were listed in Table S6. As lithium ions are removed from the layered structure, the *a*-axis lattice parameter decreases while the *c*-axis lattice parameter initially expands. According to the counterplot of XRD patterns, there is a phase change from the beginning hexagonal phase H1 to a novel hexagonal phase H2 and a coexistence of H1 and H2 during the charging process (Fig. 4b). It is worth noting that there is no formation of the H3 phase during charging, which avoids the more dramatic phase transition. The stacked XRD patterns and change of *c*-axis both provide the evidence to support this point (Fig. 4c). During discharging, there is no split of peaks suggesting that no phase change exists in this process. At the same time, the volumetric change is as small as 2.12%, much lower than previously reported.^{58, 59} In addition, the *ex-situ* XRD patterns were also performed to reveal volume changes of N-NCM and C-NCM cathode. Apparently, the as-fabricated N-NCM product has smaller volume changes than that of C-NCM (Fig. S18 and S19, Table S6 and S7). This suggests that the nanorod-like N-NCM significantly relieves phase transition and volumetric change

during Li⁺ insertion/extraction, thus suppressing the capacity fade.

Galvanostatic intermittent titration technique (GITT) surveys were conducted to evaluate the Li⁺ diffusion coefficient (D_{Li^+}) and the results provided in Fig. 5a,b. The D_{Li^+} can be calculated using the GITT diffusion equation (Fick's second law):⁶⁰

$$D_{Li^+} = \frac{4}{\pi\tau} \left(\frac{n_M V_M}{S} \right)^2 \left(\frac{\Delta V_s}{\Delta V_t} \right)^2 \left(\tau \leq \frac{L^2}{D_{Li^+}} \right) \quad (2)$$

where D_{Li^+} is the Li⁺ diffusivity (cm² s⁻¹), τ is the time duration of the pulse (s), S is the cell interfacial area (cm²), n_M and V_M are the molar mass (mol) and volume (cm³ mol⁻¹) of the active material, respectively. ΔV_s is the potential difference at the state of equilibrium (V), ΔV_t is the polarization potential (V), and L is the length of Li⁺ diffusion (cm). The single titration step of the GITT curve plus vs. cell voltage is provided in Fig. S20a,b, in which the different parameters of V_o , IR_{drop} , V_1 , V_2 , V_3 , etc. are schematically presented. The E and $\tau^{1/2}$ show a good linear relationship in Fig. S20c,d which indicates that D_{Li^+} can be estimated based on the GITT diffusion equation. The D_{Li^+} speedily increase at the beginning of charging (SOC < 20%) along with the expansion of the c parameter, thus broadening the Li⁺ diffusion path.^{24, 61} It's obvious that the D_{Li^+} of N-NCM electrode is two orders of magnitude higher than that of the C-NCM electrode during the Li⁺ desertion (charge) process (Fig. 5a,b). Moreover, the D_{Li^+} of N-NCM electrode is 4.6×10^{-8} cm² s⁻¹ at the state of 60% charge, while that of C-NCM is only 1.2×10^{-10} cm² s⁻¹. Furthermore, the N-NCM electrode is more stable than that of the C-NCM electrode during discharge processes. The thermal stabilities of the delithiated (after charging to 4.4 V at C/10) N-NCM and C-NCM electrodes were both performed by DSC and displayed close thermal stability (Fig. S21).

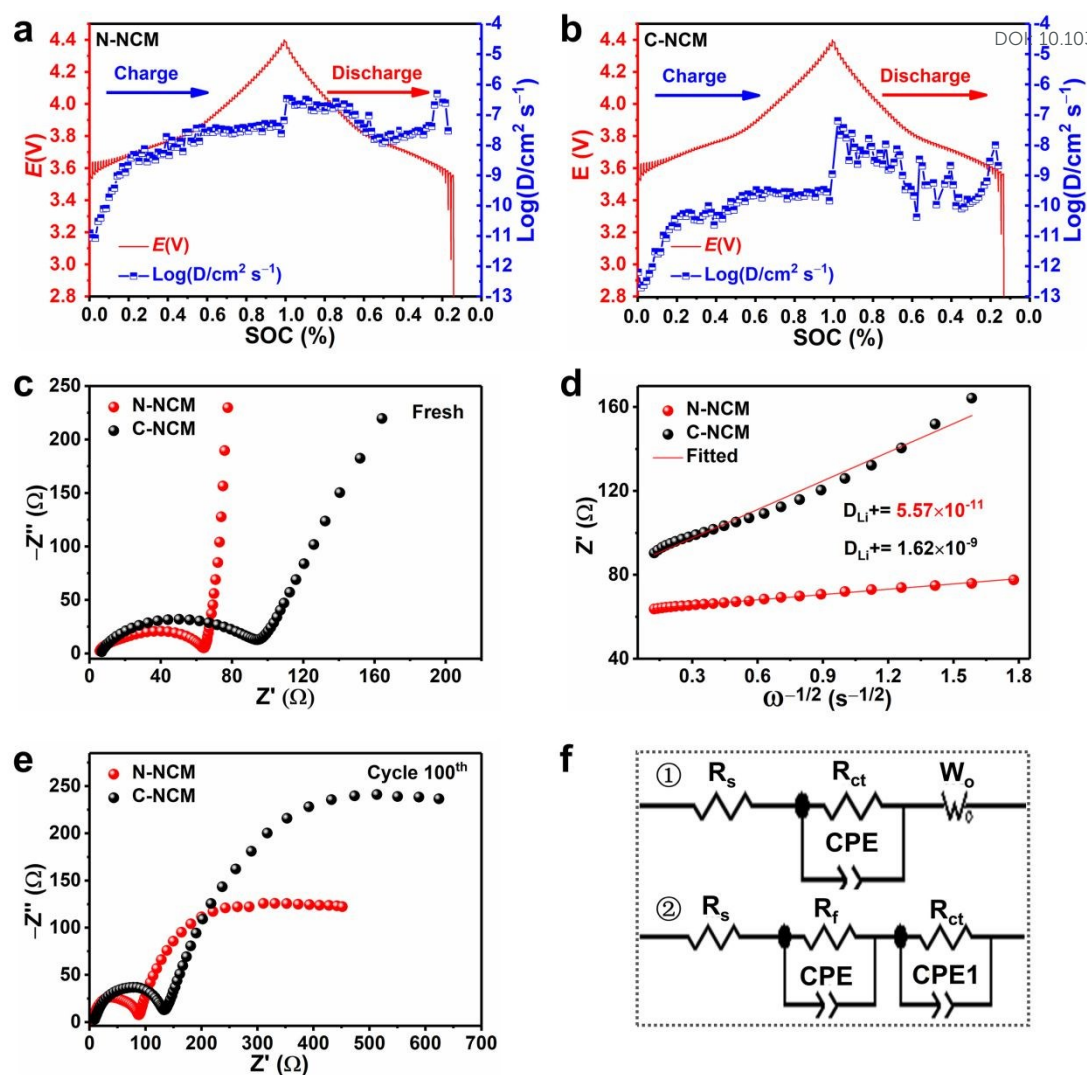


Fig. 5. (a,b) The GITT curves (red line) and Li^+ diffusion coefficients (blue line) of the N-NCM (a) and C-NCM (b) cathodes in the voltage of 2.8–4.4 V at C/10 rate. (c-e) the Nyquist plots of N-NCM and C-NCM cathodes in the fresh half-cell (c) and after 100th cycles (e) over 2.8–4.4 V at 2 C rate, and (d) shows the relation between Z' and the square root of frequency ($\omega^{-1/2}$) derived from a low-frequency region of corresponding EIS; (f) the equivalent circuits of fresh half-cell (①) and after 100th cycles (②) were used to fit the experimental data, R_s : solution resistance; R_f : surface film resistance; and R_{ct} : charge transfer resistance; CPE : constant phase element; W_o : Warburg element (open).

To further realize the difference between N-NCM and C-NCM electrodes, electrochemical impedance spectrum (EIS) tests were also performed to investigate the Li^+ diffusion coefficient. The EIS of N-NCM and C-NCM electrodes before cycling (Fig. 5c) and after 100th cycles (Fig. 5e) in 2.8–4.4 V at 2 C rate were measured and the typical Nyquist plots were further stimulated to form the equivalent circuit by Z-view software (Fig. 5f). The specific parameters are shown in Table 1. Specially, D_{Li^+} in the electrode materials is related to the straight line in the low frequency (Warburg diffusion region) abiding the following equation (3):⁶²

$$D_{\text{Li}^+} = \frac{R^2 T^2}{2A^2 n^4 F^4 C^2 \sigma^2} \quad (3)$$

$$C = \frac{3}{N_A \times V} \quad (4)$$

$$Z' = R_D + R_L + \sigma \omega^{-1/2} \quad (5)$$

Where R is the ideal gas constant, T is the absolute temperature, F is the Faraday constant, n is the number of oxidized electrons per molecule, A is the surface area of the electrode, and C is the concentration of Li^+ in the cathode, which can be calculated from formula (4) ($\text{LiNi}_{0.6}\text{Co}_{0.2}\text{Mn}_{0.2}\text{O}_2$ has a similar $\alpha\text{-NaFeO}_2$ type layered structure to LiCoO_2 with three Li-ions in a unit cell). N_A is the Avogadro constant and V is the cell volume. σ is the Warburg coefficient, related to Z' in formula (5), which is the slope in the relationship between the Z' and the square root of frequency ($\omega^{-1/2}$) (Fig. 5d). Before cycling, the R_{ct} values are about 61.3 and 79.1 Ω for N-NCM and C-NCM, respectively. Discernibly, the N-NCM cathode exhibits a smaller impedance and a higher D_{Li^+} of $1.62 \times 10^{-9} \text{ cm}^2 \text{ s}^{-1}$ than that of C-NCM ($5.57 \times 10^{-11} \text{ cm}^2 \text{ s}^{-1}$), indicating an enhanced electron and ion transport. Also, the N-NCM electrode exhibits smaller R_f

and R_{ct} values than that of the C-NCM electrode after 100 cycles. In conclusion, the smaller impedance and higher D_{Li^+} of N-NCM are attributed to nanorod-like morphology with exposed {010} active planes offering more unobstructed channels for Li-ions diffusion. In addition, the nano-sized rod shape of the N-NCM cathode dramatically reduces the Li^+ diffusion distance endowing a fast transport rate. As a result, the N-NCM cathode exhibits excellent rate performance and cycling stability. Furthermore, the detailed SEM (Fig. 6a) and TEM (Fig. 6b,c) images also confirm that the current N-NCM cathode maintained 1D nanorod structure after 200 cycles. Perfectly, there is no crack in these particles indicates outstanding structural stability during repeated cycles. Interestingly, Fig. 6d shows a nanorod with a typical crystalline orientation. It can be observed from the HRTEM image (Fig. 6e) and its corresponding SAED pattern (Fig. 6f) that the c -axis is alone in the radial direction of the N-NCM nanorod. It can be inferred that the lateral faces of the nanorod are the active {010} facets and these active {010} facets occupied a high proportion.

Table 1. Simulated results of the Nyquist plots.

Sample	Fresh			D_{Li^+} [cm^2 s^{-1}]	Cycle 100 th		
	R_s [Ω]	R_{ct} [Ω]	W_{o-R} [Ω]		R_s [Ω]	R_f [Ω]	R_{ct} [Ω]
N-NCM	4.3	61.3	1.7	1.62×10^{-9}	5.4	78.5	443.5
C-NCM	5.9	79.1	32.3	5.57×10^{-11}	7.5	126.2	766.2

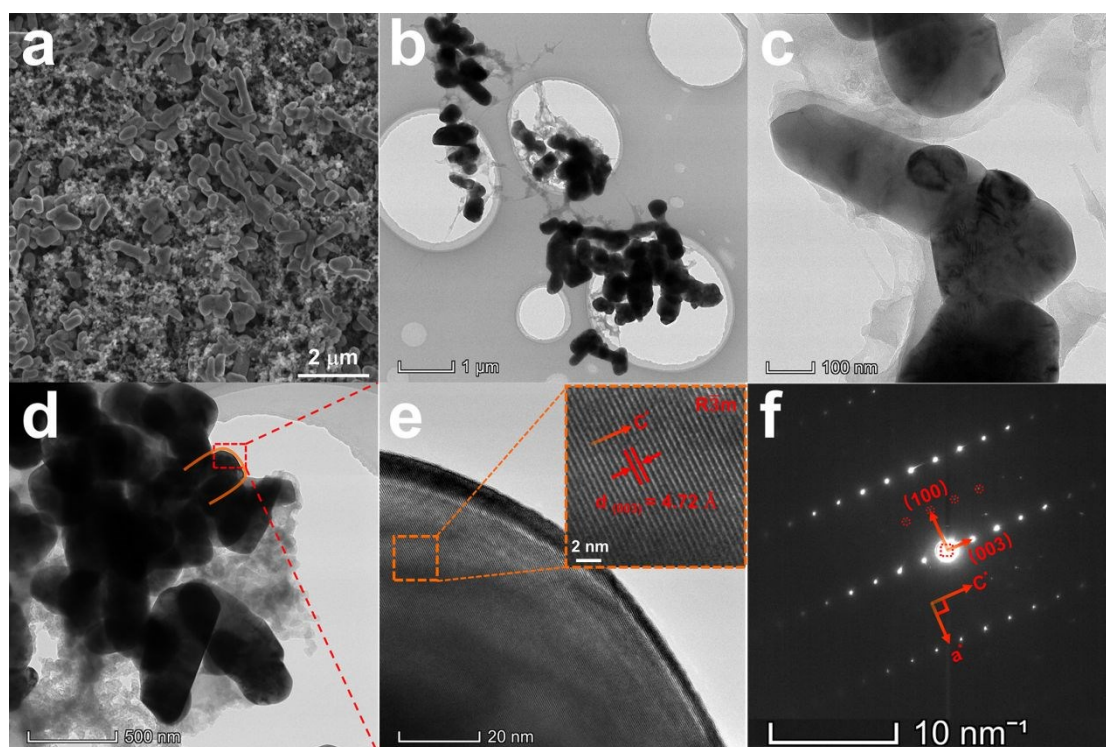


Fig. 6. Morphology and microstructure of the N-NCM cathode after cycling: (a) SEM image, (b-e) TEM and HRTEM images and (f) SAED pattern of the N-NCM cathode after 100 cycles at 2 C rate and 30 °C.

4 Conclusions

A nanorod-like $\text{LiNi}_{0.6}\text{Co}_{0.2}\text{Mn}_{0.2}\text{O}_2$ cathode has been successfully synthesized via a facial surfactant-free synthesis route. Such unique morphology makes more {010} electrochemical active plane exposed, further shorten the diffusion distance of Li^+ ions. Systematic investigations show that its diffusion kinetic is improved due to this microstructure design, as a result, it displays excellent rate performance and structural stability. In the process of cycling, this cathode could suppress the H2-H3 phase transition with an ultra-low strain of 2.12% in volume. In addition, when the rate is

raised to 5 C, this cathode still exhibits a high capacity of 152.2 mAh g⁻¹ with capacity retention of 90.6% even after 200 cycles. The superior electrochemical performance N-NCM cathode achieved lay a solid foundation for the practical application of Ni-rich materials. Meanwhile, the simple synthesis route without organic surfactants provides an avenue to obtain nanomaterials with exposed electrochemical active planes applying on the field of secondary batteries supercapacitors and catalysis.

Acknowledgments

This research was accomplished with the support from the National Natural Science Foundation of China (no. 51771076), Innovative Research Groups of the National Natural Science Foundation of China (no. NSFC51621001), and Guangdong “Pearl River Talents Plan” (no. 2017GC010218).

References

1. M. Armand and J. M. Tarascon, *Nature*, 2008, **451**, 652–657.
2. L. Zhang, X. Qin, S. Zhao, A. Wang, J. Luo, Z. L. Wang, F. Kang, Z. Lin and B. Li, *Adv. Mater.*, 2020, **32**, 1908445.
3. S. Zhao, C. D. Sewell, R. Liu, S. Jia, Z. Wang, Y. He, K. Yuan, H. Jin, S. Wang, X. Liu and Z. Lin, *Adv. Energy Mater.*, 2020, **10**, 1902657.
4. B. Jiang, C. Han, B. Li, Y. He and Z. Lin, *ACS Nano*, 2016, **10**, 2728–2735.
5. B. Jiang, Y. He, B. Li, S. Zhao, S. Wang, Y. B. He and Z. Lin, *Angew. Chem., Int. Ed.*, 2017, **56**, 1869–1872.

6. V. Etacheri, R. Marom, R. Elazari, G. Salitra and D. Aurbach, *Energy Environ. Sci.*, 2011, **4**, 3243–3262.
7. A. Konarov, S.-T. Myung and Y.-K. Sun, *ACS Energy Lett.*, 2017, **2**, 703–708.
8. H. Zhu, Y. Huang, H. Zhu, L. Wang, S. Lan, X. Xia and Q. Liu, *Small Methods*, 2020, **4**, 1900223.
9. F. Lin, I. M. Markus, D. Nordlund, T.-C. Weng, M. D. Asta, H. L. Xin and M. M. Doeff, *Nat. Commun.*, 2014, **5**, 3529.
10. W. Liu, P. Oh, X. Liu, M.-J. Lee, W. Cho, S. Chae, Y. Kim and J. Cho, *Angew. Chem., Int. Ed.*, 2015, **54**, 4440–4457.
11. J. Kim, H. Lee, H. Cha, M. Yoon, M. Park and J. Cho, *Adv. Energy Mater.*, 2018, **8**, 1702028.
12. Y. Wei, J. Zheng, S. Cui, X. Song, Y. Su, W. Deng, Z. Wu, X. Wang, W. Wang, M. Rao, Y. Lin, C. Wang, K. Amine and F. Pan, *J. Am. Chem. Soc.*, 2015, **137**, 8364–8367.
13. H. Kim, M. G. Kim, H. Y. Jeong, H. Nam and J. Cho, *Nano Lett.*, 2015, **15**, 2111–2119.
14. L. Yao, F. Liang, J. Jin, B. V. R. Chowdari, J. Yang and Z. Wen, *Chem. Eng. J.*, 2020, **389**, 124403.
15. F. Schipper, H. Bouzaglio, M. Dixit, E. M. Erickson, T. Weigel, M. Talianker, J. Grinblat, L. Burstein, M. Schmidt, J. Lampert, C. Erk, B. Markovsky, D. T. Major and D. Aurbach, *Adv. Energy Mater.*, 2018, **8**, 1701682.
16. D. Kong, J. Hu, Z. Chen, K. Song, C. Li, M. Weng, M. Li, R. Wang, T. Liu, J. Liu,

- M. Zhang, Y. Xiao and F. Pan, *Adv. Energy Mater.*, 2019, **9**, 1901756.
17. T. Weigel, F. Schipper, E. M. Erickson, F. A. Susai, B. Markovsky and D. Aurbach, *ACS Energy Lett.*, 2019, **4**, 508–516.
18. C. Zhang, J. Wan, Y. Li, S. Zheng, K. Zhou, D. Wang, D. Wang, C. Hong, Z. Gong and Y. Yang, *J. Mater. Chem. A*, 2020, **8**, 6893–6901.
19. Y.-K. Sun, S.-T. Myung, M.-H. Kim, J. Prakash and K. Amine, *J. Am. Chem. Soc.*, 2005, **127**, 13411–13418.
20. Y.-K. Sun, Z. Chen, H.-J. Noh, D.-J. Lee, H.-G. Jung, Y. Ren, S. Wang, C. S. Yoon, S.-T. Myung and K. Amine, *Nat. Mater.*, 2012, **11**, 942–947.
21. P. Yan, J. Zheng, J. Liu, B. Wang, X. Cheng, Y. Zhang, X. Sun, C. Wang and J.-G. Zhang, *Nat. Energy*, 2018, **3**, 600–605.
22. X. Zeng, C. Zhan, J. Lu and K. Amine, *Chem*, 2018, **4**, 690–704.
23. X. Xu, H. Huo, J. Jian, L. Wang, H. Zhu, S. Xu, X. He, G. Yin, C. Du and X. Sun, *Adv. Energy Mater.*, 2019, **9**, 1803963.
24. L.-P. He, K. Li, Y. Zhang and J. Liu, *ACS Appl. Mater. Interfaces*, 2020, **12**, 28253–28263.
25. Z. Zheng, X.-D. Guo, S.-L. Chou, W.-B. Hua, H.-K. Liu, S. X. Dou and X.-S. Yang, *Electrochim. Acta*, 2016, **191**, 401–410.
26. H. Liu, G. Liang, C. Gao, S. Bi, Q. Chen, Y. Xie, S. Fan, L. Cao, W. K. Pang and Z. Guo, *Nano Energy*, 2019, **66**, 104100.
27. Y. Lee, M. G. Kim and J. Cho, *Nano Lett.*, 2008, **8**, 957–961.
28. J. Liu, K. Song, C. Zhu, C.-C. Chen, P. A. van Aken, J. Maier and Y. Yu, *ACS*

Nano, 2014, **8**, 7051–7059.

View Article Online
DOI: 10.1039/D0TA10608A

29. K. Yu, X. Pan, G. Zhang, X. Liao, X. Zhou, M. Yan, L. Xu and L. Mai, *Adv. Energy Mater.*, 2018, **8**, 1802369.
30. X. Xu, J. Liu, Z. Liu, Z. Wang, R. Hu, J. Liu, L. Ouyang and M. Zhu, *Small*, 2018, **14**, 1800793.
31. J. Liu, X. Xu, J. Shen, F. Li, Z. Wang, D. Zhang and S. Zuo, *Chem- Eur J*, 2020, **26**, 14708–14714.
32. J. Lu, Q. Peng, W. Wang, C. Nan, L. Li and Y. Li, *J. Am. Chem. Soc.*, 2013, **135**, 1649–1652.
33. T. Jin, Q. Han, Y. Wang and L. Jiao, *Small*, 2018, **14**, 1703086.
34. J. Kasnatscheew, M. Evertz, B. Streipert, R. Wagner, R. Klöpsch, B. Vortmann, H. Hahn, S. Nowak, M. Amereller, A. C. Gentschev, P. Lamp and M. Winter, *Phys. Chem. Chem. Phys.*, 2016, **18**, 3956–3965.
35. Z. Chen, D. Chao, J. Liu, M. Copley, J. Lin, Z. Shen, G.-T. Kim and S. Passerini, *J. Mater. Chem. A*, 2017, **5**, 15669–15675.
36. X. Ju, H. Huang, W. He, H. Zheng, P. Deng, S. Li, B. Qu and T. Wang, *ACS Sustainable Chem. Eng.*, 2018, **6**, 6312–6320.
37. Y. Xiao, P.-F. Wang, Y.-X. Yin, Y.-F. Zhu, Y.-B. Niu, X.-D. Zhang, J. Zhang, X. Yu, X.-D. Guo, B.-H. Zhong and Y.-G. Guo, *Adv. Mater.*, 2018, **30**, 1803765.
38. J. Meng, H. Xu, Q. Ma, Z. Li, L. Xu, Z. Chen, B. Cheng and S. Zhong, *Electrochim. Acta*, 2019, **309**, 326–338.
39. J. Zeng, Y. Cui, D. Qu, Q. Zhang, J. Wu, X. Zhu, Z. Li and X. Zhang, *ACS Appl.*

- Mater. Interfaces*, 2016, **8**, 26082–26090.
40. G. Z. Wei, X. Lu, F. S. Ke, L. Huang, J. T. Li, Z. X. Wang, Z. Y. Zhou and S. G. Sun, *Adv. Mater.*, 2010, **22**, 4364–4367.
41. F. Fu, G.-L. Xu, Q. Wang, Y.-P. Deng, X. Li, J.-T. Li, L. Huang and S.-G. Sun, *J. Mater. Chem. A*, 2013, **1**, 3860–3864.
42. R. Yu, X. Zhang, T. Liu, X. Xu, Y. Huang, G. Wang, X. Wang, H. Shu and X. Yang, *ACS Sustainable Chem. Eng.*, 2017, **5**, 8970–8981.
43. J. J. N. Rodriguez-Carvajal, 2001, **26**, 12.
44. G. Ma, S. Li, W. Zhang, Z. Yang, S. Liu, X. Fan, F. Chen, Y. Tian, W. Zhang, S. Yang and M. Li, *Angew. Chem., Int. Ed.*, 2016, **55**, 3667–3671.
45. J. Zhao, W. Zhang, A. Huq, S. T. Misture, B. Zhang, S. Guo, L. Wu, Y. Zhu, Z. Chen, K. Amine, F. Pan, J. Bai and F. Wang, *Adv. Energy Mater.*, 2017, **7**, 1601266.
46. H. Yu, Y.-G. So, Y. Ren, T. Wu, G. Guo, R. Xiao, J. Lu, H. Li, Y. Yang, H. Zhou, R. Wang, K. Amine and Y. Ikuhara, *J. Am. Chem. Soc.*, 2018, **140**, 15279–15289.
47. L. Zhang, N. Li, B. Wu, H. Xu, L. Wang, X.-Q. Yang and F. Wu, *Nano Lett.*, 2015, **15**, 656–661.
48. M. Xu, L. Fei, W. Zhang, T. Li, W. Lu, N. Zhang, Y. Lai, Z. Zhang, J. Fang, K. Zhang, J. Li and H. Huang, *Nano Lett.*, 2017, **17**, 1670–1677.
49. M. Chen, X. Jin, Z. Chen, Y. Zhong, Y. Liao, Y. Qiu, G. Cao and W. Li, *J. Mater. Chem. A*, 2019, **7**, 13120–13129.
50. M. Jiang, Q. Zhang, X. Wu, Z. Chen, D. L. Danilov, R.-A. Eichel and P. H. L.

- Notten, *ACS Appl. Energy Mater.*, 2020, **3**, 6583–6590.
51. S. Zhao, Z. Wang, Y. He, B. Jiang, Y. Harn, X. Liu, F. Yu, F. Feng, Q. Shen and Z. Lin, *ACS Energy Lett.*, 2016, **2**, 111–116.
52. S. Zhao, Z. Wang, Y. He, H. Jiang, Y. W. Harn, X. Liu, C. Su, H. Jin, Y. Li, S. Wang, Q. Shen and Z. Lin, *Adv. Energy Mater.*, 2019, **9**, 1901093.
53. S.-U. Woo, C. S. Yoon, K. Amine, I. Belharouak and Y.-K. Sun, *J. Electrochem. Soc.*, 2007, **154**, A1005.
54. E. Flores, P. Novák, U. Aschauer and E. Berg, *Chem. Mater.*, 2019, **32**, 186–194.
55. H. Li, A. Liu, N. Zhang, Y. Wang, S. Yin, H. Wu and J. R. Dahn, *Chem. Mater.*, 2019, **31**, 7574–7583.
56. K. Sahni, M. Ashuri, Q. He, R. Sahore, I. D. Bloom, Y. Liu, J. A. Kaduk and L. L. Shaw, *Electrochim. Acta*, 2019, **301**, 8–22.
57. F. Xin, H. Zhou, X. Chen, M. Zuba, N. Chernova, G. Zhou and M. S. Whittingham, *ACS Appl. Mater. Interfaces*, 2019, **11**, 34889–34894.
58. H.-H. Ryu, K.-J. Park, C. S. Yoon and Y.-K. Sun, *Chem. Mater.*, 2018, **30**, 1155–1163.
59. H. H. Sun, H.-H. Ryu, U.-H. Kim, J. A. Weeks, A. Heller, Y.-K. Sun and C. B. Mullins, *ACS Energy Lett.*, 2020, **5**, 1136–1146.
60. Z. Shen, L. Cao, C. D. Rahn and C. Y. Wang, *J. Electrochem. Soc.*, 2013, **160**, A1842–A1846.
61. H. Zhou, F. Xin, B. Pei and M. S. Whittingham, *ACS Energy Lett.*, 2019, **4**, 1902–1906.

62. Y. T. Ma, P. F. Liu, Q. S. Xie, G. B. Zhang, H. F. Zheng, Y. X. Cai, Z. Li, L. S. Wang, Z. Z. Zhu, L. Q. Mai and D. L. Peng, *Nano Energy*, 2019, **59**, 184–196.

[View Article Online](#)

DOI: 10.1039/D0TA10608A

TOC

View Article Online
DOI: 10.1039/D0TA10608A

Nanorod-like Ni-rich $\text{LiNi}_{0.6}\text{Co}_{0.2}\text{Mn}_{0.2}\text{O}_2$ possesses more exposed active {010} facets and the volume change of lithiation/delithiation is as small as 2.12%.

